

Relationship Between Ascending Thoracic Aortic Aneurysms Hemodynamics and Biomechanical Properties

Francesca Condemì , Salvatore Campisi, Magalie Viallon, Pierre Croisille, and Stéphane Avril 

Abstract—Objective: Ascending thoracic aortic aneurysm (aTAA) is a major cause of human deaths. Despite important recent progress to better understand its pathogenesis and development, the role played by deranged hemodynamics on aTAA risk of rupture is still partially unknown. Our aim was to develop and apply a novel methodology to assess the correlation between aTAA rupture risk and hemodynamic biomarkers combining for the first time *in vivo*, *in vitro*, and *in silico* analyses. **Methods:** Computational fluid dynamic analyses were performed and validated on ten patients using patient-specific data derived from CT scan and four-dimensional MRI. Systolic wall shear stress, time-averaged wall shear stress (TAWSS), flow eccentricity ($\text{Flow}_{\text{eccentricity}}$), and helicity intensity (h_2) were assessed. A bulge inflation test was carried out *in vitro* on the ten aTAA samples resected during surgical repair. The biomechanical and rupture properties of these samples were derived: the burst pressure, the physiological tangent elastic modulus (E_{physio}), the Cauchy stress at rupture (σ_{rupt}), the rupture stretch (λ_{rupt}), and the rupture stretch criterion ($\Upsilon^{\text{stretch}}$). Statistical analysis was performed to determine correlation between all variables. **Results:** Statistically highly significant ($p < 0.01$) positive correlation between λ_{rupt} and the TAWSS ($r = 0.867$ and $p = 0.001$) was found. **Conclusion:** This study shows that relatively low TAWSS significantly correlates with reduced rupture properties in aTAAs. **Significance:** Understanding the pathogenesis of aTAA remains crucial to reduce morbidity and mortality. Our aim is to establish possible correlations between aTAA rupture risk and hemodynamic biomarkers by combining for the first time *in vivo*, *in vitro*, and *in silico* analyses.

Index Terms—Ascending thoracic aortic aneurysm, CFD, 4D MRI, risk of rupture, rupture stretch, TAWSS.

Manuscript received December 28, 2018; revised February 25, 2019 and May 20, 2019; accepted June 17, 2019. Date of publication July 16, 2019; date of current version March 19, 2020. This work was supported by the European Research Council (ERC Grant bioloanomics, under Grant 647067). (Corresponding author: Stéphane Avril.)

F. Condemì was with Mines Saint-Etienne, with Université Lyon, with Université Jean Monnet, and also with Inserm. She is now with Université Toronto.

S. Campisi is with the CHU Hôpital Nord.

M. Viallon and P. Croisille are with Université Lyon, and also with Université Jean Monnet.

S. Avril is with Mines Saint-Etienne CIS-EMSE, SAINBIOSE, F-42000 Saint Etienne, France, with the INSERM, U1059, F-42000 Saint Etienne, France, with the Université de Lyon, SAINBIOSE, F-42000 Saint Etienne, France, and also with Université Jean Monnet, SAINBIOSE, F-42023 Saint-Etienne, France (e-mail: avril@emse.fr).

Digital Object Identifier 10.1109/TBME.2019.2924955

I. INTRODUCTION

THE aorta is the largest artery of the human body. The proximal part of the aorta, from the aortic valve to the brachiocephalic trunk, is called the ascending thoracic aorta (aTA) [1]. When the diameter of the aTA overly expands or when the aTA abnormally bulges, an ascending thoracic aortic aneurysm (aTAA) is formed. Dissections and sudden ruptures are the two main risks for patients with an aTAA, with a very high mortality rate due to the extreme severity of hemorrhage conditions in this territory [2]. Untreated ascending aortic dissections within 48 hours are followed by death in approximately 50% patients [3]. To avoid fatal events, prophylactic surgery is the recommendation even though the elective surgery lowers mortality to only 3–5% [3]. Therefore, understanding the pathogenesis of aTAA remains crucial to reduce the morbidity and mortality, the aim being to derive relevant biomarkers permitting to plan elective surgery repairs as timely as possible.

Although hemodynamics likely plays an important role in the pathogenesis of cardiovascular diseases [4], [5], the role of deranged hemodynamics on the mechanical and rupture properties of the aortic walls is still partially unknown. Advanced insight in imaging techniques have enabled acquiring detailed anatomical images and *in vivo* hemodynamic information in large arteries. High resolution dynamic CT imaging, for example, has been employed to build finite element models (FEM) and to obtain information about the biomechanical properties of the wall tissue [6], [7]. However, although this useful non-invasive technique provides important information on aTAA mechanics, it does not provide functional insight on aTAA hemodynamics.

4D flow MRI has become very commonplace for quantitative analysis of the aortic hemodynamics [8]. It has been used to assess the wall shear stress (WSS) *in vivo*, along with bulk flow structures which may be involved in aneurysm formation [9]. Despite the tremendous progress permitted by 4D flow MRI, its spatial resolution remains a limitation, preventing to derive accurate gradients of the blood velocities close to the aortic wall, and then lacking accuracy to derive hemodynamic descriptors based on these gradients. This can be overcome using computational fluid dynamics (CFD) which is acknowledged as the most accurate approach for the derivation of velocity gradients close to the aortic wall. The downside of CFD though is that it is purely computational, requiring a precise definition of geometries and a fine tuning of boundary conditions to achieve

patient-specific predictions. Combining 4D flow MRI and CFD is then an excellent compromise as the CFD model can be set up using 4D flow MRI datasets to define the geometries and to tune the boundary conditions [10].

The current challenge is now to apply these techniques for establishing possible universal effects relating hemodynamic descriptors and the wall mechanical and rupture properties derived from *in vitro* tests on real patient tissues.

Relationships between WSS patterns and wall mechanical properties may stem from the regulatory role of vascular cells through mechanotransduction. It has been known for many years that endothelial cells sense the WSS and can stimulate relaxation in vascular smooth muscle cells by nitric oxide signaling for instance. This permits maintaining a rather uniform time-average WSS (TAWSS) of about 1 Pa across all arteries at vascular homeostasis. Conversely, disruption of this vascular homeostasis, with for instance low and dispersed WSS values, is known to be atheroprone. In the context of aTAA, Michel *et al.* [9] submitted that low and dispersed WSS values may also accelerate the advection of plasma proteins through the aortic wall, which could interact with vSMCs and components of the extracellular matrix (ECM). The outward convection of blood-borne plasminogen through the wall, further converted to active plasmin at the vSMC membrane, can induce vSMC disappearance, proteolysis of adhesive proteins and activation of MMPs. This results in a decrease of elastic properties, the tissue becoming stiffer and less extensible.

Recently Guzzardi *et al.* [11] showed that regions of increased WSS correspond with ECM dysregulation and elastic fiber degeneration in the ascending aorta of bicuspid valve (BAV) patients, implicating valve-related hemodynamics as a contributing factor in the development of aortopathy. Their WSS values were derived directly from 4D flow MRI data without using CFD.

In the present study, based on our previous work, [12] we combine for the first time together *in vivo* 4D flow MRI and *in silico* CFD models to analyze the aortic flow patterns, the WSS and the TAWSS distribution of 10 aTAA patients for whom we subsequently characterized the mechanical and rupture properties of their aTAA after surgical resection. The goal is to look closer at the possible correlations between hemodynamic descriptors and wall properties.

II. MATERIAL AND METHODS

A. Patient Recruitment

All procedures performed in this study were in accordance with the ethical standards of the 1964 Helsinki declaration and its later amendments. The study was approved by the Institutional Review Board of the University Hospital center of Saint-Étienne (France). After providing informed consent, 10 patients hosting an aneurysmal aTA had their thorax scanned first with a computed tomography (CT) gated scanner and then with a 3T MRI scanner with a 4D flow sequence. Each patient subsequently underwent an open surgical procedure of aTAA repair during which the bulged part of their aTA was resected and characterized on a biomechanical bench test. All procedures were

TABLE I
PATIENTS' DEMOGRAPHIC INFORMATION

Patient	Age	Aortic valve morphology	Valvulopathy	d (mm)
1	58	BAV	AI grade 4+	53
2	68	TAV	AI grade 4+	49
3	77	BAV	AI grade 4+	55
4	70	TAV	AI grade 4+	41
5	58	TAV	Physiologic	55
6	83	TAV	AI grade 2+	57
7	73	TAV	Physiologic	70
8	45	BAV	AS	56
9	76	TAV	AI grade 4+	45
10	82	TAV	AI grade 2+	43

BAV = bicuspid aortic valve; TAV = tricuspid aortic valve; AI grade 4+ = severe aortic insufficiency; AI grade 2+ = moderate aortic insufficiency; AS = aortic stenosis; d = diameter in the region of the bulge.

performed at the University Hospital Center of Saint-Étienne (France).

Demographic information are reported in Table I.

B. In Vivo Data Acquisition

The preoperative ECG gated CT scans provided images of each patient's thoracic anatomy at ten different phases of the cardiac cycle (DICOM images resolution: 512x512, slice thickness = 0.5 mm). The 3T MRI scanner (Siemens Magnetom Prisma) provided images of each patient's thoracic anatomy and blood flows. A 4D flow phase-contrast sequence [13] was employed as in [10].

C. Geometry and Mesh Reconstruction

Patient-specific tridimensional geometries of the aortic arch, the aortic branches (brachiocephalic artery, BCA, left common carotid artery, LCC, and left subclavian artery, LSUB) and the descending aorta (DescAo) were reconstructed from CT scans using a semi-automatic segmentation in the CRIMSON (Cardiovascular Integrated Modelling and Simulation) software. Unstructured meshes, consisting of 1.5–6.2 millions of tetrahedral elements, were generated using ANSYS Mesh (v17.2, ANSYS Inc., Canonsburg, PA). A convergence analysis was carried out to obtain mesh independent analyses.

The aorta was partitioned in three segments, including the aTA Segment of Interest (aTASoI), as: 1) segment A which nearly extends until the sinotubular junction, 2) segment B which approximately corresponds to the dilated aTA resected during surgery (aTASoI) and 3) segment C which includes the aortic arch and the descending aorta until the diaphragm. We also defined the middle cross sectional plane which divides this aTASoI in two equal halves (Fig. 1A). This plane of interest, further denoted PoI, permitted to evaluate the velocity profiles of the blood at this very specific location. All the post-processing analyses carried out to extract the WSS-based descriptors focused on the luminal wall of the aTASoI portion. To define the location of the WSS hotspots along the aTAA, the aTASoI was represented as flat square piece obtained through a cut in the axial direction (in the direction of blood flow) at the level of the

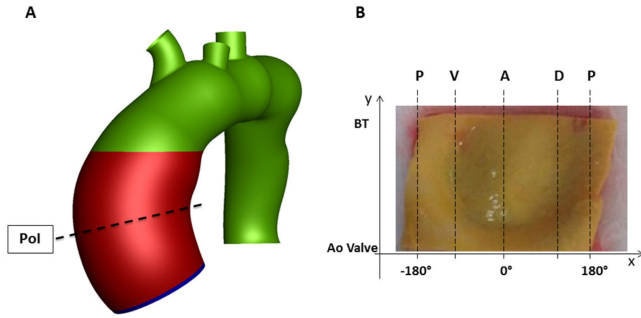


Fig. 1. (A) The three aortic segments are shown: 1) segment A which nearly extends until the sinotubular junction (in blue), 2) segment B which approximately corresponds to the dilated aTA resected during surgery (aTASol in red) and 3) segment C which includes the aortic arch and the descending aorta until the diaphragm (in green). The middle cross sectional plane divides the aTASol in two equal halves (Pol). (B) The aTASol was considered as flat square piece. Along the x axis, the aTASol was partitioned in four regions consisting of: 1) a dorsal region (D), 2) a ventral region (V), an anterior region (A) and a posterior region (P). Along the y axis, the aTASol extends from the aortic valve (Ao Valve) to the brachiocephalic trunk (BT).

inner curvature. Then this flat square piece was partitioned in four regions consisting of: 1) a dorsal region (D), 2) a ventral region (V), an anterior region (A) and a posterior region (P, in Fig. 1B).

D. Boundary Conditions

3D time-varying patient-specific velocity profiles were extracted from the *in vivo* 4D MRI acquisitions as in [10]. At the supra-aortic branches, the extracted patient-specific flow waveforms were imposed as outlet boundary conditions. Finally, a finely tuned Windkessel model was used as outlet boundary condition at the descending aorta. To avoid adverse impact on the ascending aorta hemodynamics, the outlet length was extended so that a nearly unidirectional flow could be obtained at the extended outlet position.

Aortic walls were assumed to be rigid and impermeable, and a no-slip condition, $v_{\text{wall}} = 0$, was used.

E. Numerical Resolution

A laminar flow was assumed and the blood was modeled as non-Newtonian using the Carreau model [10]. The Navier-Stokes equations were solved across the aortic lumen in ANSYS Fluent (v17.2, ANSYS, Canonsburg, PA, USA) using the Semi-Implicit Method for Pressure-Linked Equations (SIMPLE) algorithm. A second-order interpolation scheme was chosen for calculating cell-face pressures and a second-order upwind interpolation scheme was applied. Several cardiac cycles were solved until a periodic solution was reached, and the results obtained in the last cycle were used for the analysis.

Finally, a second order implicit time advanced scheme was used as transient-time solver and a time step of 1 ms was chosen for the simulations. At each time step, the iterative resolution was stopped when the scaled residuals reached a value lower than 10^{-4} .

F. Flow Helicity, Flow Eccentricity, and Wall Shear Stress Analysis

The CFD-calculated velocity profiles were verified against the 4D MRI-measured velocities. For that, we extracted from the Fluent postprocessor the velocity maps averaged throughout the cardiac cycle in the PoI of the aTASol whereas the averaged velocity maps at the same location were extracted from the 4D MRI datasets with Ensight. The flow eccentricity ($\text{Flow}_{\text{eccentricity}}$) was calculated in Matlab, such as [14]:

$$\text{Flow}_{\text{eccentricity}} = \frac{\sqrt{\sum_j (C_j - C_{\text{vel}_j})^2}}{D} \quad j = x, y, z \quad (1)$$

where C_j is the coordinate of the center of the lumen, C_{vel_j} is the “center of velocity” and D is the diameter. The “center of velocity”, C_{vel_j} , was calculated as the weighted barycenter of the cross section, each position being weighted by the absolute velocity value [14]. The flow is qualified as centrally distributed with respect to the vessel centerline for $\text{Flow}_{\text{eccentricity}}$ values equal to 0. The flow is qualified as eccentric for $\text{Flow}_{\text{eccentricity}}$ equal to 1 [14].

The h_2 index was calculated to define the helicity intensity in the aTASol region of the aortic volume [15], [16].

The peak WSS was defined as the highest wall shear stress in the mesh at the systolic peak. The maximum TAWSS was obtained as [10]:

$$\text{TAWSS} = \frac{1}{T} \int_0^T \text{WSS} \, dt \quad (2)$$

where T is the period of the cardiac cycle and WSS is the instantaneous wall shear stress.

The 90-percentile WSS and TAWSS was computed by removing 10% of all nodes containing the peak stress values. Being the mesh built with elements of the same size, this corresponds to 10% of the surface area. Therefore, the maximum stress of the remaining nodes is defined as the 90-percentile stress.

G. In Vitro Bulge Inflation Test

The 10 aTAA samples collected after surgical procedures were characterized mechanically using our *in vitro* bulge inflation bench test [17]. A flat square piece of tissue (about 40x40 mm²) was cut from the greater curvature of each aTAA specimen in the axial direction. Then, our bulge inflation test device [17] was used for clamping the sample during the inflation until the rupture occurred. During the test, the pressure was monitored using a digital manometer (WIKA, DG-10) and images of the sample, previously spayed with an appropriate dye, were recorded using a DIC system to reconstruct the 3D deformations fields of the inflated aortic sample. The ARAMIS (GOM, v. 6.2.0) software was used to derive these deformation fields from the collected images and Matlab was used to derive the biomechanical properties of interest from the deformation fields.

Four properties of interest were introduced [17]:

- 1) The Cauchy stress at rupture (σ_{rup}).
- 2) The Rupture stretch (λ_{rup})
- 3) The Rupture stretch criterion ($\Upsilon_{stretch}$)

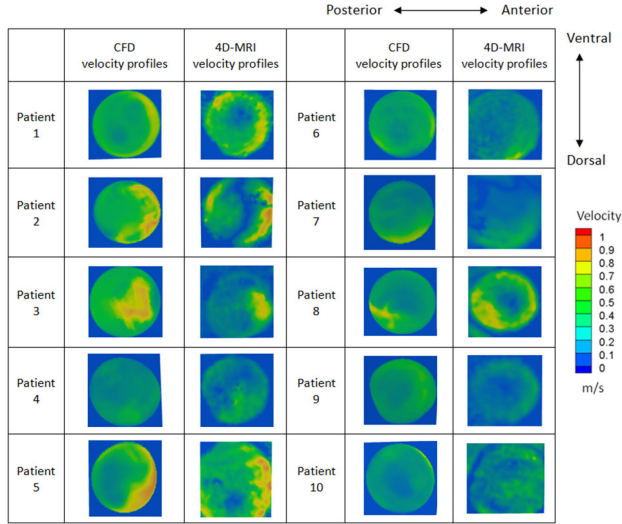


Fig. 2. Time-averaged velocity profiles 4D MRI-measured (on the right-hand side) and CFD-calculated (on the left-hand side). The dorsal, ventral, anterior and posterior side are defined according to Fig. 1B.

4) The physiological tangent elastic modulus (E_{physio})

They were all derived here on top of the burst pressure which was recorded using the WIKA, DG-10 manometer.

H. Statistical Analysis

For each of the 10 patients, our CFD results were quantitatively compared to the time-averaged velocity profiles obtained with 4D flow MRI at the PoI cross-sectional plane, corresponding to the location of maximum dilatation. More specifically we performed a statistical comparison of the $Flow_{eccentricity}$ evaluated by both techniques (CFD and 4D flow MRI). To assess the agreement between the CFD-calculated and the 4D MRI-measured quantities, a Bland Altman plot was done [18].

A normality test was performed using Shapiro-Wilk test for the parametric inference, to determine whether the sample came from a population which had a normal distribution. A pre-determined level of significance equal to 95% ($p \geq 0.05$) was considered. Parametric and non-parametric statistical analyses were performed accordingly using, respectively, Pearson and Spearman correlation method. A 95% (statistically significant) and a 99.9% (statistically highly significant) confidence intervals were considered to assess the relationships between hemodynamic indicators (WSS, TAWSS, h_2 and $Flow_{eccentricity}$) and biomechanical wall properties (σ_{rupt} , λ_{rupt} , $\Upsilon_{stretch}$, E_{physio} and burst pressure).

The statistical analysis was performed using the Minitab software.

III. RESULTS

A. Comparison Between CFD-Calculated vs. 4D MRI-Measured Velocities and Flows

For qualitative comparison, the time-averaged velocity profiles derived from CFD and 4D flow MRI are shown in Fig. 2. The $Flow_{eccentricity}$ at PoI showed a good agreement

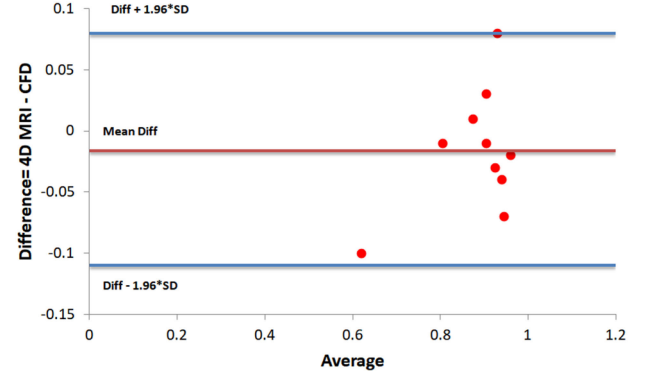


Fig. 3. Bland-Altman plot comparing the CFD and 4D flow MRI $Flow_{eccentricity}$ derived from the time-averaged velocity profiles at PoI. Blue lines show 95% confidence lower and upper bands and red line shows mean difference value.

between the two sets of data. For the quantitative comparison, the average error between CFD-calculated and 4D flow MRI-measured time-averaged $Flow_{eccentricity}$ was evaluated and was found equal to $3.98 \pm 5.06\%$.

Moreover, Bland-Altman plot comparing the CFD and 4D flow MRI $Flow_{eccentricity}$ at PoI is shown in Fig. 3. Most of data points calculated at the systolic peak remain in the 95% limit bands, which indicates good agreement between the MRI measurements and the CFD predictions.

B. Hemodynamic Descriptors

Two models (Patient 5 and Patient 7) showed a peak WSS located in the dorsal side of the aTASoI region with a maximum value of, respectively, 22 Pa and 8 Pa. In one model (Patient 4) the highest WSS was found in the ventral side of the aTASoI with a maximum value of 11 Pa. The rest had the peak WSS situated in the anterior side of the aTASoI. The range of the peak WSS was of 14.6 ± 6.4 Pa. The 90-percentile of the WSS which was considered in the statistical analysis ranged between 11.3 Pa and 2.1 Pa with a mean value of 5.3 ± 3.2 Pa. Three patients (Patient 4, Patient 5 and Patient 7) showed a peak TAWSS in the dorsal side of the aTASoI with a maximum value of, respectively, 2.5 Pa, 8 Pa and 3.5 Pa. The other patients had their peak TAWSS located in the anterior region of the aTASoI region. The maximum TAWSS was equal to 4.1 ± 1.7 Pa. The 90-percentile of the maximum TAWSS was of 2.7 ± 0.9 Pa. The WSS and the TAWSS contours are presented, respectively, in Fig. 4 and in Fig. 5. The CFD results are summarized in Table II.

C. Wall Material Properties

Table III summarizes the bulge inflation test results, as previously reported by Duprey *et al.* [17]. The samples showed the dissection-like mode of rupture with failure of the media and delamination between the media and the adventitia.

Although the adventitia was preserved and the aorta could still bear some load, the ultimate stress and the ultimate stretch were measured when the media ruptured. The average value of σ_{rupt} , λ_{rupt} , $\Upsilon_{stretch}$ and E_{physio} were, respectively, equal

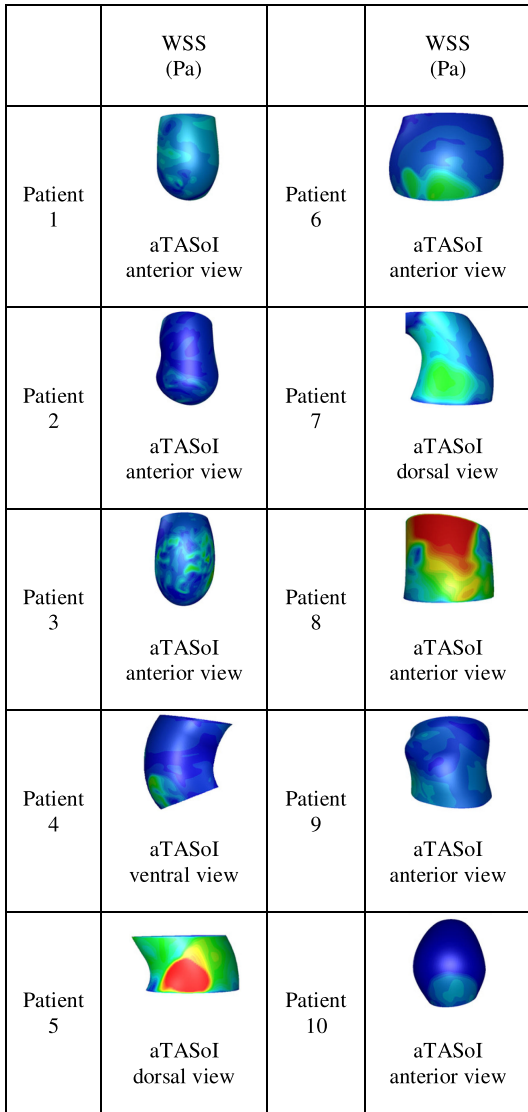


Fig. 4. The distribution of the 90th percentile of the CFD-calculated WSS_{max} along the aTASoI is shown for all the ten patients. The dorsal, ventral, anterior and posterior side are defined according to Fig. 1B.

TABLE II
CFD-CALCULATED VS. 4D MRI-MEASURED RESULTS

Patient	CFD-calculated results				4D MRI-measured results		
	WSS_{max} (Pa)	$TAWSS_{max}$ (Pa)	h_2	Flow rate [l/min]	Time-averaged Flow _{eccentricity} [l/min]	Flow rate [l/min]	Time-averaged Flow _{eccentricity} [l/min]
1	4.50	3.10	10.74	17.40	0.91	17.80	0.98
2	3.90	2.81	3.58	11.40	0.92	11.70	0.96
3	6.40	2.90	7.71	25.10	0.80	25.80	0.81
4	4.00	1.48	2.22	12.50	0.97	12.60	0.89
5	10.00	5.00	5.64	22.00	0.92	22.50	0.89
6	4.20	2.12	7.79	22.00	0.91	24.00	0.94
7	5.07	2.47	3.24	11.40	0.88	11.90	0.87
8	11.30	2.50	3.82	14.20	0.95	13.20	0.97
9	1.37	2.80	3.46	14.60	0.90	16.00	0.91
10	2.10	2.00	3.88	11.40	0.57	12.00	0.67
Avg.	5.28	2.72	5.21	16.20	0.87	16.75	0.89
±SD	±3.17	±0.94	±2.71	±5.13	±0.11	±5.48	±0.09

CFD-calculated WSS_{max} , $TAWSS_{max}$, h_2 and maximum flow rate at systole. The CFD-calculated vs. the 4D MRI-measured Flow_{eccentricity} and flow rate are compared. The average values and the standard deviation are calculated.

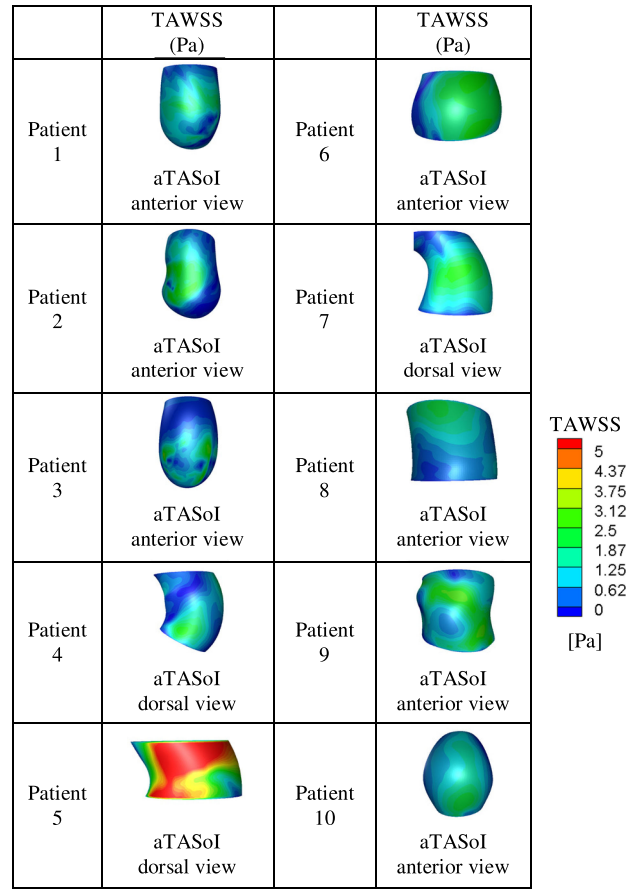


Fig. 5. The distribution of the 90th percentile of the CFD-calculated $TAWSS_{max}$ along the aTASoI is shown for all the ten patients. The dorsal, ventral, anterior and posterior side are defined according to Fig. 1B.

TABLE III
BULGE INFLATION TEST RESULTS

Patient	σ_{rupt} (MPa)	λ_{rupt}	$\gamma_{stretch}$	E_{physio}	Burst Pressure (kPa)
1	1.11	1.53	0.84	0.61	138
2	0.80	1.49	0.93	1.55	80
3	2.46	1.48	0.89	1.30	200
4	0.39	1.30	0.95	1.80	80
5	2.30	1.60	0.88	0.93	155
6	0.54	1.32	0.93	1.66	100
7	0.97	1.37	0.89	1.35	119
8	2.91	1.47	0.86	0.94	229
9	0.78	1.42	0.94	2.10	92
10	0.50	1.39	0.96	3.00	82
Avg.±	1.28±	1.44±	0.91±	1.52±	127.50±
SD	0.92	0.09	0.04	0.68	52.80

σ_{rupt} is the rupture stress; λ_{rupt} is the rupture stretch; $\gamma_{stretch}$ is the rupture stretch criteria; E_{physio} is the physiological tangent elastic modulus.

to 1.28 ± 0.92 MPa, 1.44 ± 0.09 , 0.91 ± 0.04 and 1.52 ± 0.92 . The burst pressure at rupture ranged between 80 kPa and 229 kPa. No correlation between the aneurysm diameter and the ultimate stress values and the ultimate stretch values was found. However, σ_{rupt} , $\gamma_{stretch}$ and E_{physio} correlated with

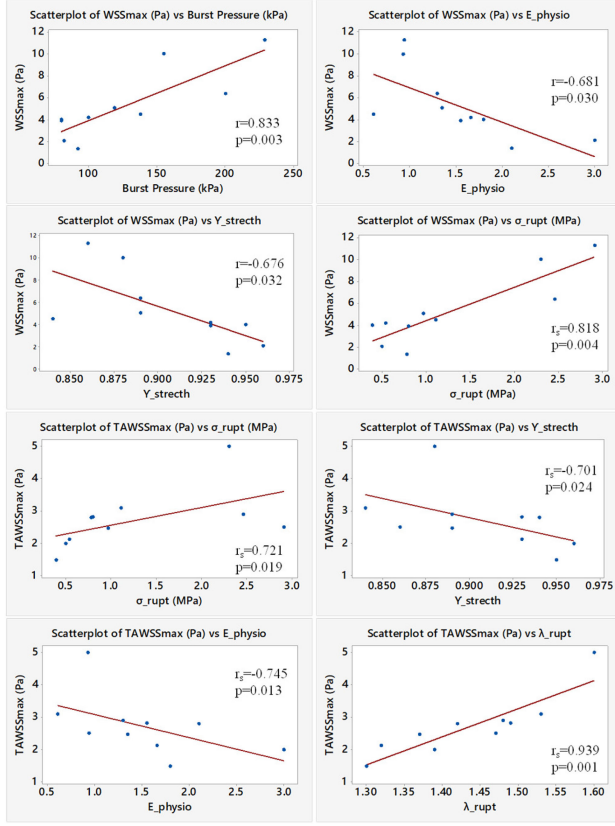


Fig. 6. The results of the statistical analysis show the correlation between hemodynamic and biomechanical descriptors calculated using parametric and non-parametric statistical analyses, respectively, Pearson (r) and Spearman (r_s) correlation method.

the patients' age. The σ_{rupt} and the λ_{rupt} values were also compared statistically between BAV and TAV patients, but no significant trend was observed [17].

D. Correlation Between WSS and Wall Mechanical Properties

A normal distribution was satisfied for: λ_{rupt} , $\Upsilon_{stretch}$, E_{physio} , burst pressure, WSS_{max} and h_2 .

The Pearson correlation method showed a statistically significant ($p < 0.05$) positive correlation between WSS_{max} and the burst pressure ($r = 0.833$ and $p = 0.003$). A statistically significant ($p < 0.05$) negative correlation was found between WSS_{max} and, respectively, E_{physio} ($r = -0.681$ and $p = 0.030$) and $\Upsilon_{stretch}$ ($r = -0.676$ and $p = 0.032$).

Spearman rho method showed a statistically significant ($p < 0.05$) positive correlation between WSS and σ_{rupt} ($r_s = 0.818$ and $p = 0.004$).

A statistically significant ($p < 0.05$) positive correlation was found between TAWSS and σ_{rupt} ($r_s = 0.721$ and $p = 0.019$), while a negative correlation ($p < 0.05$) was found with $\Upsilon_{stretch}$ ($r_s = -0.701$ and $p = 0.024$) and E_{physio} ($r_s = -0.745$ and $p = 0.013$). Statistically highly significant ($p < 0.001$) positive correlation was found between TAWSS and λ_{rupt} ($r_s = 0.939$ and $p = 0.001$). Interestingly, no correlation was found between

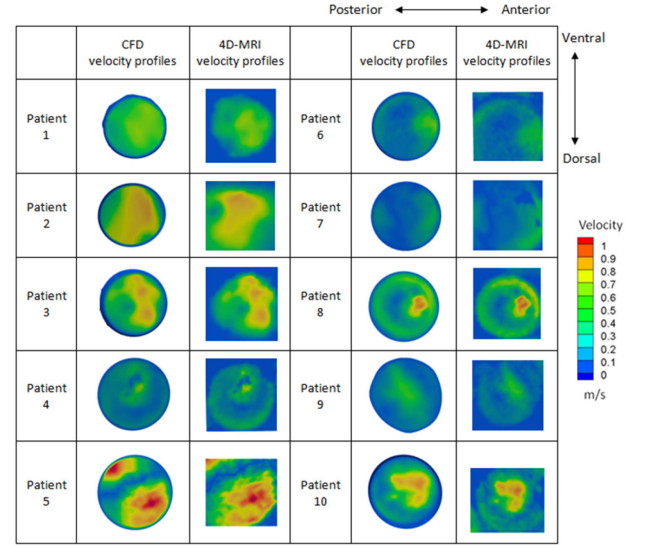


Fig. 7. Time-averaged velocity profiles derived from 4D MRI (on the right-hand side) and boundary conditions assigned at the aortic inlet of the CFD model (on the left-hand side).

λ_{rupt} and the peak WSS at systole. Figure 6 summarizes the statistical analysis results.

IV. DISCUSSION

In this study, we investigated for the first time the possible correlation between hemodynamic descriptors and wall properties in aTAAs combining 4D flow MRI, biomechanical tests and CFD numerical modelling. CFD numerical analyses were systematically defined and verified using 4D flow MRI in vivo data. A statistical analysis showed a strong correlation between the time-averaged wall shear stress predicted by CFD and the rupture stretch measured in the biomechanical tests.

A. About WSS and TAWSS

Deranged aTAA hemodynamics likely plays an important role in altering the arterial morphology. In this context, attention has been paid to the tangential load exerted by blood flow on the aortic walls, well known as wall shear stress. In particular, altered distribution of WSS and deranged blood flow has been related to aortic valve morphological and functional lesions [10]. Our CFD results, in good agreement with the time-averaged 4D MRI data, showed high $Flow_{eccentricity}$ in all patients analyzed. Elevated $Flow_{eccentricity}$ was associated to high values of WSS and TAWSS. Seven out of ten patients analyzed (exception for Patient 4, Patient 5 and Patient 7) showed WSS and TAWSS hotspots in the anterior side of the aTASol region.

It reconciles with previous results showing that flow impingement against the aneurysmal walls generates a non-homeostatic distribution of the WSS in the bulge region [10]. However, the magnitude and the location of the maximum WSS can vary along the four sides of the aTASol (D, V, A and P) due to the flow inclination at the inlet, i.e., the neck angle between the plane of the inlet cross section and the transverse plane of the thorax, and the morphology of the aortic valve [10].

B. About the Correlation of WSS and TAWSS With Aortic Wall Biomechanics

Understanding the relationship between hemodynamics descriptors and rupture risk is not a trivial issue and there is still a pressing need to conduct research on their possible correlation for potential application in clinical prognosis. Therefore, the aim of our study was to establish a methodology to assess the potential correlation between the rupture risk and hemodynamics biomarkers combining *in vivo*, *in vitro* and *in silico* analyses. Our statistical results showed a significant positive correlation between σ_{rupt} and, respectively, the WSS_{max} and the $TAWSS_{max}$. Moreover, a strong positive correlation was found between λ_{rupt} and $TAWSS_{max}$. Both statistical results suggest that relatively low TAWSS may have negative effects on aneurysm strength [19]. Chooi *et al.* [20] showed that low residence time reduces the water flux and the advection of macromolecules into and across the arterial wall. Moreover, low WSS has been shown to disturb endothelial cells in a number of locations of the arterial tree (cerebral aneurysms, coronaries) which may induce a larger permeability of the wall. It is well known that larger TAWSS is often associated with lower residence time of particles. Therefore, our findings lead to the hypothesis that relatively higher TAWSS may induce a “washing effect”, limiting this advection of macromolecules. The phenomenon of “outward convection” was recently defined by Michel *et al.* [9]. They showed that it is dependent on hemodynamic factors, such as pressure and wall shear stress, and on the aortic properties, such as permeability. More specifically, this biomechanical phenomenon results into blood-borne plasminogen infiltrating in the arterial wall. This may induce a proteolytic injury and cause damage of the extracellular matrix, in particular elastin. This would explain why the higher ultimate stress were found for aTAA exposed to higher WSS and weaker properties (lower rupture stretch) were obtained for aTAA having smaller values of TAWSS. According with these trends, the WSS_{max} and the $TAWSS_{max}$ negatively correlate with $\Upsilon_{stretch}$ and E_{physio} . This $\Upsilon_{stretch}$ criteria ranges between 0 and 1. The closer it is to 1, the larger is the risk of rupture. From our results, high value of $\Upsilon_{stretch}$ are associated to lower WSS_{max} and $TAWSS_{max}$. However, these results still need to be confirmed on a larger cohort and also to be reconciled with the results of Guzzardi *et al.* [11] who showed more elastin damage in the ascending aorta of BAV patients in the regions exposed to larger WSS. However, these studies cannot be directly compared considering that Guzzardi *et al.* [11] looked at regional correlations between WSS and elastin proteolysis whereas our study found inter-individual correlations between WSS and rupture properties. Moreover, in our study the population of patients was not stratified in two different groups considering BAV and TAV patients.

Our study showed also that it is relevant to define aTAA rupture using a maximum stretch criterion although the maximum stress criterion is commonly used for the rupture of other types of aneurysms [21]. Whereas the peak wall stress was shown to estimate patient risk with a higher accuracy, sensitivity, and specificity for patients with abdominal aortic aneurysms (AAAs) [22], Trabelsi *et al.* [23] supported the sig-

nificance of stretch-based rupture criteria in aTAAs. Moreover, their results showed that a failure criterion based on the *in vitro* ultimate stretch was significantly correlated with the aortic extensile stiffness derived from *in vivo* distensibility [24].

Overall, the rupture of an aTAA is highly complex and it is preceded by a multifactorial process of alteration of the aortic wall combining: i) biomechanical factors, ii) biochemical factors and iii) hemodynamic factors (including WSS). Elastin fragmentation and faster collagen turnover are the main alterations occurring in aTAA pathogenesis and development. It was shown in mice models that this leads to a decrease of the aortic maximum axial stretch, to a decreased aortic distensibility and an increased aortic arch pulse wave velocity [17], [25]. Therefore, it is evident that these effects, which can be summarized as a global stiffening effect, make the tissue more prone to rupture in an overstretch situation. For instance, it is reported that aneurysm rupture or dissections often occur due to severe emotional stress or physical exertion, which can provoke acute rise of the aortic blood volume [26]. Generally, the aorta can adapt its diameter in response to flow variations using vasoactivity combined with its native remarkable elasticity, thus avoiding large increase of the blood pressure [27]. However, less compliant aneurysms cannot sustain such changes of aortic blood volumes due to emotional stress, and the blood pressure can become very high [26]. Eventually, wall stretches exceeding the capacity of the aortic wall to sustain overstretch would be responsible for the initiation of dissections.

It is still important to remember that such spontaneous overstretch of the aortic wall is concomitant with a sudden rise of the blood pressure but it would never be directly related to WSS. Overpressure is likely to provoke a spontaneous aTAA rupture, [28] while WSS is expected to play a role in the longterm aTAA wall remodeling, possibly associated to the phenomenon of “outward convection” rather than rupture.

C. Limitations/Future Works

Several limitations exist in this work and should be addressed before considering translation to the clinical setting.

The first limitation is the small number of patients included in the analysis. However, we are currently achieving longitudinal studies on a larger cohort in order to evaluate the role exerted by WSS in the wall remodeling process.

The second limitation concerns our rupture risk criterion which was established *in vitro* and not *in vivo*. To address this limitation, we are developing a new method enabling the non-invasive characterization of local biomechanical properties of the aorta based on medical imaging analysis [7], [23], [24].

Moreover, our numerical model used to calculate the hemodynamic descriptors (WSS and TAWSS) relies on a number of assumptions. The first assumption concerns the rigid walls. The second assumption is that it satisfies the velocity distributions measured by 4D MRI at the inlet. Both assumptions may induce errors in the computed velocity fields and the deduced instantaneous WSS, especially due to noise in the 4D MRI data. Actually, our main conclusion (strong correlation between λ_{rupt} and $TAWSS_{max}$) focused on the time-averaged WSS more

than on the instantaneous WSS at the systolic peak. TAWSS is calculated by integrating the instantaneous WSS over the time, therefore it eliminates any temporal effect and smooths the noise effects. We also plan to add FSI analysis in further studies.

The third assumption is that we neglected the use of direct numerical simulations (DNS) to properly resolve turbulences. However, according to previous analysis, [29] the TAWSS distribution between high resolution (HR) and Normal Resolution (NR) simulations are comparable.

The fourth assumption is that we did not low-sampled the high resolution CFD flow estimates to the low resolution 4D MRI meshes before calculating the $\text{Flow}_{\text{eccentricity}}$ error between the two sets of data. We plan to resample the CFD mesh in a further study.

Moreover, any possible relationships between turbulent quantities (e.g., turbulent kinetic energy) and strength were not evaluated. We plan to achieve further analysis related to turbulence effects in a future study.

Finally, the study did not include the aortic valve geometry and the aortic-valve leaflets motion over the cardiac cycle. However, the inflow boundary conditions at the inlet of the aorta were extracted from 4D MRI to define patient-specific maps of velocity profiles, as described in the “Materials and Methods” section.

V. CONCLUSION

In summary, a novel methodology, combining for the first time 4D flow MRI data, biomechanical tests and CFD modeling, was established to evaluate the correlation between hemodynamic descriptors and biomechanical properties in aTAAs. Our results showed a strong positive correlation between the rupture stretch and the time average wall shear stress. Longitudinal studies on larger cohorts are still needed to confirm how hemodynamic biomarkers correlates with aneurysm progression.

ACKNOWLEDGMENT

The authors would like to thank Dr. A. J. Barker and Dr. M. Markl from the Northwestern University of Chicago (Chicago, IL, USA) who provided insight and expertise for the 4D MRI data analysis. They would also like to thank SIEMENS Healthineers for providing 4D flow acquisition sequences and collaboration support. They thank Dr. Morbiducci and Dr. Gallo from the Polytechnic of Turin (Turin, Italy) who provided insight and expertise that greatly assisted the CFD modeling and data analysis. They are also grateful to Ansys, Inc., for providing Ansys-Fluent (ANSYS Academic Research, Release 17.2). *Conflict of interest statement:* The authors confirm that there are no conflict of interest related with this publication.

REFERENCES

- [1] R. Erbel and H. Eggebrecht, “Aortic dimensions and the risk of dissection,” *Heart (Brit. Cardiac Soc.)*, vol. 92, pp. 137–142, 2006.
- [2] R. R. Davies *et al.*, “Yearly rupture or dissection rates for thoracic aortic aneurysms: simple prediction based on size,” *Ann. Thoracic Surgery*, vol. 73, pp. 17–28, 2002.
- [3] M. P. Prakash *et al.*, “Ascending aortic aneurysms: Pathophysiology and indications for surgery,” *E-J. Eur. Soc. Cardiol. Council Cardiol. Pract.*, vol. 10, no. 7, 2011.
- [4] Y. S. Chatzizisis *et al.*, “Role of endothelial shear stress in the natural history of coronary atherosclerosis and vascular remodeling,” *Mol., Cellular, Vascular Behav.*, vol. 49, pp. 2379–2393, 2007.
- [5] A. A. Owida *et al.*, “Numerical analysis of coronary artery bypass grafts: An over view,” *Comput. Methods Programs Biomed.*, vol. 108, pp. 689–705, 2012.
- [6] O. Trabelsi *et al.*, “Predictive models with patient specific material properties for the biomechanical behavior of ascending thoracic aneurysms,” *Ann. Biomed. Eng.*, vol. 44, pp. 84–98, Jan. 1, 2016.
- [7] S. Farzaneh *et al.*, “Inverse identification of local stiffness across ascending thoracic aortic aneurysms,” *Biomech. Model. Mechanobiol.*, vol. 18, no. 1, pp. 137–153, Feb. 2019.
- [8] M. Markl *et al.*, “4D flow MRI,” *J. Magn. Reson. Imag.*, vol. 36, pp. 1015–1036, 2012.
- [9] J.-B. Michel *et al.*, “From genetics to response to injury: vascular smooth muscle cells in aneurysms and dissections of the ascending aorta,” *Cardiovascular Res.*, vol. 114, pp. 578–589, 2018.
- [10] F. Condemi *et al.*, “Fluid- and biomechanical analysis of ascending thoracic aorta aneurysm with concomitant aortic insufficiency,” *Ann. Biomed. Eng.*, vol. 45, pp. 2921–2932, Dec. 1, 2017.
- [11] D. G. Guzzardi *et al.*, “Valve-related hemodynamics mediate human bicuspid aortopathy: Insights from wall shear stress mapping,” *J. Amer. College Cardiol.*, vol. 66, pp. 892–900, 2015.
- [12] F. Condemi *et al.*, “Ascending thoracic aorta aneurysm repair induces positive hemodynamic outcomes in a patient with unchanged bicuspid aortic valve,” *J. Biomech.*, vol. 16, 2018, pp. 145–148.
- [13] C. Strecker *et al.*, “Flow-sensitive 4D MRI of the thoracic aorta: Comparison of image quality, quantitative flow, and wall parameters at 1.5 T and 3 T,” *J. Magn. Reson. Imag.*, vol. 36, pp. 1097–1103, Nov. 2012.
- [14] M. Sigovan *et al.*, “Comparison of four-dimensional flow parameters for quantification of flow eccentricity in the ascending aorta,” *J. Magn. Reson. Imag.*, vol. 34, pp. 1226–1230, Nov. 2011.
- [15] U. Morbiducci *et al.*, “In vivo quantification of helical blood flow in human aorta by time-resolved three-dimensional cine phase contrast magnetic resonance imaging,” *Ann. Biomed. Eng.*, vol. 37, pp. 516–531, 2009.
- [16] D. Gallo *et al.*, “Helical flow in carotid bifurcation as surrogate marker of exposure to disturbed shear,” *J. Biomech.*, vol. 45, pp. 2398–2404, 2012.
- [17] A. Duprey *et al.*, “Biaxial rupture properties of ascending thoracic aortic aneurysms,” *Acta Biomaterialia*, vol. 42, pp. 273–285, 2016.
- [18] D. G. Altman and J. M. Bland, “Measurement in medicine: the analysis of method comparison studies,” *Statistician*, vol. 32, pp. 307–317, 1983.
- [19] J. Bürk *et al.*, “Evaluation of 3D blood flow patterns and wall shear stress in the normal and dilated thoracic aorta using flow-sensitive 4D CMR,” *J. Cardiovascular Magn. Reson.*, vol. 14, p. 84, 2012.
- [20] K. Chooi *et al.*, “Intimal and medial contributions to the hydraulic resistance of the arterial wall at different pressures: A combined computational and experimental study,” *J. Roy. Soc. Interface*, vol. 13, 2016, Art. no. 20160234.
- [21] A. Valencia *et al.*, “Fluid structural analysis of human cerebral aneurysm using their own wall mechanical properties,” *Comput. Math. Methods Med.*, vol. 2013, 2013, Art. no. 293128.
- [22] Z.-Y. Li *et al.*, “Association between aneurysm shoulder stress and abdominal aortic aneurysm expansion: A longitudinal follow-up study,” *Circulation*, vol. 122, pp. 1815–1822, 2010.
- [23] O. Trabelsi *et al.*, “A non-invasive methodology for ATAA rupture risk estimation,” *J. Biomech.*, vol. 66, pp. 119–126, 2018.
- [24] S. Farzaneh *et al.*, “Identifying local arterial stiffness to assess the risk of rupture of ascending thoracic aortic aneurysms,” *Ann. Biomed. Eng.*, vol. 47, pp. 1–13, 2019.
- [25] A. Redheuil *et al.*, “Age-related changes in aortic arch geometry: Relationship with proximal aortic function and left ventricular mass and remodeling,” *J. Amer. College Cardiol.*, vol. 58, pp. 1262–1270, 2011.
- [26] C. de Virgilio *et al.*, “Ascending aortic dissection in weight lifters with cystic medial degeneration,” *Ann. Thoracic Surgery*, vol. 49, pp. 638–642, 1990.
- [27] J. Humphrey, *Cardiovascular Solid Mechanics: Cells, Tissues, and Organs*. New York, NY, USA: Springer, 2002.
- [28] R. Campobasso *et al.*, “Evaluation of peak wall stress in an ascending thoracic aortic aneurysm using FSI simulations: Effects of aortic stiffness and peripheral resistance,” *Cardiovascular Eng. Technol.*, vol. 9, pp. 707–722, Oct. 19, 2018.
- [29] K. Valen-Sendstad and D. A. Steinman, “Mind the gap: Impact of computational fluid dynamics solution strategy on prediction of intracranial aneurysm hemodynamics and rupture status indicators,” *Amer. J. Neuro-radiol.*, vol. 35, pp. 536–543, 2014.